

First-principles transition-state tensorial cluster expansion of vacancy diffusion in Ta-W beyond the kinetically-resolved activation approximation

Jacob Jeffries ^{*1}, Brianna Sebastian-Olazabal², and Enrique Martinez ^{†1,2}

¹Department of Materials Science and Engineering, Clemson University, Clemson, SC 29634, USA

²School of Mechanical and Automotive Engineering, Clemson University, Clemson, SC 29634, USA

May 25, 2026

Abstract

Predicting diffusion in chemically complex alloys remains challenging due to the strong dependence of migration barriers on local atomic environments. Here, we develop a first-principles-informed framework that directly learns environment-dependent migration barriers without relying on reduced kinetic approximations such as the kinetically resolved activation (KRA) model. Migration barriers computed using density functional theory and nudged elastic band calculations are represented via a tensorial cluster expansion including transition states and deployed in on-lattice kinetic Monte Carlo simulations. Applied to the Ta-W system, the framework captures nontrivial composition-dependent diffusion behavior arising from a crossover between solute trapping and percolated low-barrier transport pathways, yielding a maximum in the apparent activation energy near intermediate compositions. This approach establishes a general and scalable route for integrating first-principles transition-state energetics into mesoscale kinetic simulations, enabling predictive multiscale modeling of diffusion in chemically complex materials and providing a pathway for uncovering emergent transport phenomena.

1 Introduction

High-throughput screening of concentrated alloys is necessary for the discovery and development of damage-resistant materials for clean energy applications. Primarily, the effects of radiation on materials are driven by point defect (PD)-mediated diffusion, underpinning phase stability, precipitation, segregation, and radiation response^[1-4]. Of particular research interest are radiation-induced segregation^[5-7] and radiation-induced precipitation^[8-10], which generate inhomogeneities that can negatively affect material response, and are controlled by kinetic parameters such as transport coefficients.

Particularly promising candidates for structural materials are refractory high entropy alloys^[11-15]. As such, understanding and modeling PD-mediated diffusion in refractory high entropy alloys, and concentrated alloys in general, is necessary for alloy discovery for advanced applications. Modeling PD-

mediated diffusion in these systems is nontrivial due to the large variations in local chemical environments seen by the diffusing PD over time^[16,17]. The conventional approach to modeling PD-mediated diffusion in these systems is to fit the energy barrier of a single PD hop using the kinetically-resolved action (KRA) expression^[18-20]:

$$\Delta E = E_{\text{KRA}} + \frac{E' - E^\circ}{2} \quad (1)$$

where E_{KRA} is a fitting parameter, which may depend on local chemical environment, E° and E' are respectively the beginning and final energies along the reaction coordinate of the hop, and ΔE is the energy barrier for the hop. Then, energies are fit as a function of local chemical embeddings, usually with the cluster expansion (CE) technique^[21,22] and density functional theory (DFT) calculations^[23,24] or otherwise atomistic data. Therefore, if the KRA ex-

pression is suitably accurate, and we have sufficient first-principles data to fit a KRA model, we can easily run kinetic Monte Carlo (KMC) simulations^[25] to compute kinetic quantities of interest, e.g. diffusion coefficients and transport coefficients.

A particular success of the KRA expression is that all the quantities within the expression are independent of direction along the transition pathway, making it very well-suited for CE models. Then, the only directionality is encoded within the last term, which can be interpreted as a thermodynamic driving force. Thus, to then recover asymmetric energy barriers, it must be true that ΔE is at least moderately correlated with $E' - E^\circ$.

In this work, we find that this assumption is not met for vacancy hopping in Ta-W alloys computed using the nudged elastic band method (NEB) method^[26–29] and DFT. We additionally hypothesize that this correlation is weak in other concentrated alloys. As such, it is advantageous to not rely on a model such as the KRA, which assumes such correlations, and instead compute energy barriers directly from some embedding of local chemistry.

To achieve this, we extend our prior work on tensor cluster expansion (TCE) models^[30] by introducing a multi-lattice composed of both equilibrium sites, as well as midway points between equilibrium sites, allowing us to treat transition states as distinct configurations in an extended configuration space, enabling KMC simulations of diffusion in chemically complex alloys beyond the limitations of KRA-based approaches.

We then fit this extended model to vacancy migration in Ta-W using first-principles data using a lower-dimensional embedding of the migration data, showcasing an effective clustering of vacancy migration pathways. Lastly, we then use our fitted model to compute diffusivity over a large temperature and composition range, finding four categorically distinct regimes over composition. Notably, we find that dilute Ta inhibits vacancy diffusion up to a percolation threshold, and that dilute W leaves vacancy diffusion largely unaffected.

2 Model

First, following a previously developed tensorial cluster expansion model^[30], we write our energy as a linear function of the number of n 'th order α - β pairs and

the number of n 'th order α - β - γ three body clusters:

$$E(\mathbf{X}) = \frac{1}{2!} \varepsilon_{\alpha\beta}^{(n)} N_{\alpha\beta}^{(n)}(\mathbf{X}) + \frac{1}{3!} \zeta_{\alpha\beta\gamma}^{(n)} M_{\alpha\beta\gamma}^{(n)}(\mathbf{X}) \quad (2)$$

where $N_{\alpha\beta}^{(n)}$ is the number of α - β pairs of n 'th order, $M_{\alpha\beta\gamma}^{(n)}$ is the number of α - β - γ triplets of n 'th order, and $\varepsilon_{\alpha\beta}^{(n)}$ and $\zeta_{\alpha\beta\gamma}^{(n)}$ are their respective interaction energies. Here, both cluster count features depend on the configuration \mathbf{X} . With respect to the lower indices, all of the above tensors are symmetric, necessitating the overcounting factors $1/2!$ and $1/3!$. This can be more easily cast as a simple linear problem:

$$E(\mathbf{X}) = \mathbf{j}^\top \mathbf{t}(\mathbf{X}) \quad (3)$$

where \mathbf{X} describes the occupation of each lattice site on a static lattice:

$$X_{i\alpha} = \begin{cases} 1 & \text{site } i \text{ is occupied by atom type } \alpha \\ 0 & \text{else} \end{cases} \quad (4)$$

which allows us to calculate the counts of each cluster type as polynomials in \mathbf{X} :

$$\begin{aligned} N_{\alpha\beta}^{(n)}(\mathbf{X}) &= A_{ij}^{(n)} X_{i\alpha} X_{j\beta} \\ M_{\alpha\beta\gamma}^{(n)}(\mathbf{X}) &= B_{ijk}^{(n)} X_{i\alpha} X_{j\beta} X_{k\gamma} \end{aligned} \quad (5)$$

where $A_{ij}^{(n)}$ and $B_{ijk}^{(n)}$ are symmetric tensors encoding the topology of the lattice:

$$\begin{aligned} A_{ij}^{(n)} &= \begin{cases} 1 & (i, j) \in n\text{'th nearest neighbors} \\ 0 & \text{else} \end{cases} \\ B_{ijk}^{(n)} &= \begin{cases} 1 & (i, j, k) \in n\text{'th order triplets} \\ 0 & \text{else} \end{cases} \end{aligned} \quad (6)$$

Then, \mathbf{t} is a column vector containing the cluster counts:

$$\mathbf{t}(\mathbf{X}) = (\text{vec}(\mathbf{N}(\mathbf{X}))^\top \quad \text{vec}(\mathbf{M}(\mathbf{X}))^\top)^\top \quad (7)$$

and \mathbf{j} is a learnable column vector of interaction parameters:

$$\mathbf{j} = \left(\frac{1}{2!} \text{vec}(\boldsymbol{\varepsilon})^\top \quad \frac{1}{3!} \text{vec}(\boldsymbol{\zeta})^\top \right)^\top \quad (8)$$

For a given reaction pathway $\mathbf{X}^\circ \rightarrow \mathbf{X}^\ddagger \rightarrow \mathbf{X}'$, respectively denoting the initial, transition, and final states, the transition rate can be approximated by harmonic transition state theory (HTST)^[31]:

$$r = \nu \exp \left(-\frac{E^\ddagger - E^\circ}{k_B T} \right) \quad (9)$$

where E^\ddagger and E° are respectively the energies of the transition and initial states, and ν is an attempt frequency. Rather than predict absolute energies, we can instead use the feature vector differences to predict energy differences directly, similarly to Musa et al.^[32]. This naturally fits into the description above, in which we need energy barriers to run KMC, i.e. energy differences between initial and saddle states. We can model the energy barrier using the feature vectors above:

$$\begin{aligned} E^\ddagger - E^\circ &= \mathbf{j}^\top (\mathbf{t}(\mathbf{X}^\ddagger) - \mathbf{t}(\mathbf{X}^\circ)) \\ &= \mathbf{j}^\top (\mathbf{t}^\ddagger - \mathbf{t}^\circ) \end{aligned} \quad (10)$$

which is a generalized broken bond model, since the first k^2 elements of $\mathbf{t}^\ddagger - \mathbf{t}^\circ = \mathbf{t}(\mathbf{X}^\ddagger) - \mathbf{t}(\mathbf{X}^\circ)$ represent the pairwise interactions at the initial state that are broken at the transition state, where k is the number of chemical species in the system. From our prior work, we can also compute this feature vector difference as a function of local topology^[30], significantly reducing the computational cost of predicting the energy barrier. This feature vector difference is:

$$\begin{aligned} \Delta \tilde{N}_{\alpha\beta}^{(n)} &= \sum_{d \in \mathcal{D}} A_{dj}^{(n)} X_{d\alpha}^\ddagger X_{j\beta}^\ddagger \\ &\quad - \sum_{d \in \mathcal{D}} A_{dj}^{(n)} X_{d\alpha}^\circ X_{j\beta}^\circ \\ \Delta N_{\alpha\beta}^{(n)} &= 2\Delta \tilde{N}_{(\alpha\beta)}^{(n)} \\ \Delta \tilde{M}_{\alpha\beta\gamma}^{(n)} &= \sum_{d \in \mathcal{D}} B_{djk}^{(n)} X_{d\alpha}^\ddagger X_{j\beta}^\ddagger X_{k\gamma}^\ddagger \\ &\quad - \sum_{d \in \mathcal{D}} B_{djk}^{(n)} X_{d\alpha}^\circ X_{j\beta}^\circ X_{k\gamma}^\circ \\ \Delta M_{\alpha\beta\gamma}^{(n)} &= 3\Delta \tilde{M}_{(\alpha\beta\gamma)}^{(n)} \\ \mathbf{t}^\ddagger - \mathbf{t}^\circ &= \begin{pmatrix} \text{vec}(\Delta \mathbf{N}) \\ \text{vec}(\Delta \mathbf{M}) \end{pmatrix} \end{aligned} \quad (11)$$

where parenthesis denote symmetrization of the tensor, and $\mathcal{D} = \{i : \mathbf{X}_i^\ddagger \neq \mathbf{X}_i^\circ\}$ is the set of lattice sites that change between the initial and transition states. This model additionally obeys detailed balance, which is necessary for correctly sampling the Boltzmann distribution^[33]. Namely, consider a reaction pathway $\mathbf{X}^\circ \rightarrow \mathbf{X}^\ddagger \rightarrow \mathbf{X}'$ and its corresponding reverse reaction pathway $\mathbf{X}' \rightarrow \mathbf{X}^\ddagger \rightarrow \mathbf{X}^\circ$. Then:

$$\begin{aligned} p(\mathbf{X}^\circ) r(\mathbf{X}^\circ \rightarrow \mathbf{X}') &= \frac{1}{Z} e^{-\beta \mathbf{j}^\top \mathbf{t}^\circ} \nu e^{-\beta \mathbf{j}^\top (\mathbf{t}^\ddagger - \mathbf{t}^\circ)} \\ &= \frac{\nu}{Z} e^{-\beta \mathbf{j}^\top \mathbf{t}^\ddagger} \\ &= \frac{1}{Z} e^{-\beta \mathbf{j}^\top \mathbf{t}'} \nu e^{-\beta \mathbf{j}^\top (\mathbf{t}^\ddagger - \mathbf{t}')} \\ &= p(\mathbf{X}') r(\mathbf{X}' \rightarrow \mathbf{X}^\circ) \end{aligned} \quad (12)$$

where $p(\mathbf{X})$ denotes the probability of a state, $r(\mathbf{X} \rightarrow \mathbf{Y})$ denotes the rate of a transition, and $Z = \sum_{\mathbf{X}^\circ} e^{-\beta \mathbf{j}^\top \mathbf{t}(\mathbf{X}^\circ)}$ is the partition function of the system.

In conventional CE-based treatments of diffusion, the CE is typically used to describe the energies of stable initial and final lattice configurations, while the transition state is not treated as an independent configuration with its own cluster representation. This is typically addressed by correlating the transition state energy with the initial and final energies of the transition (i.e. the KRA relation), and using this correlation to approximate the barrier for that transition. This approach assumes that the local energetics of the initial and final states provide a reliable proxy for the energetics of the transition state. In the present work, we find that this correlation is weak at best, motivating a formulation in which the transition state itself is explicitly decorated with a feature vector, rather than its energetics inferred solely from the endpoint configurations.

In this work, we augment configuration space by creating a multi-lattice that includes both a standard lattice and a transition state lattice, allowing us to decorate the initial, transition, and final states of a vacancy hop within the same feature space. These transition state lattice sites sit in-between the standard lattice sites, allowing the hopping atom to occupy space between the standard lattice sites during a vacancy hop. In body-centered cubic (bcc) crystal structures, for example, the unit cell of such a multi-lattice is the ordinary bcc lattice positions

($\{(0, 0, 0), (1/2, 1/2, 1/2)\}$) with transition state lattice positions around the central atom in the directions of its nearest neighbors, i.e. $(1/2, 1/2, 1/2) + \frac{1}{4}(\pm 1, \pm 1, \pm 1)$ (Figure 1). Note that this specific augmented configuration space is tailored specifically to first nearest neighbor hops in bcc solids, i.e. vacancy hops along $\langle 111 \rangle$ directions. However, one could include additional transition state lattice sites for other hops, e.g. $(0, 0, 1/2)$ points for diffusion along $\langle 100 \rangle$ directions in bcc solids. However, in this work, we only account for diffusion along $\langle 111 \rangle$ directions, since diffusion along these directions is more favorable than along $\langle 100 \rangle$ directions in pure W^[34].

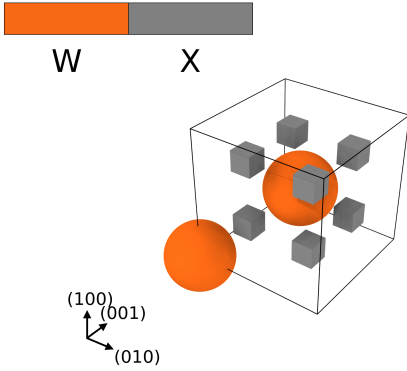


Figure 1: BCC multi-lattice including transition states with the ordinary BCC sites denoted by tungsten (W) and the transition state sites denoted by X, rendered with Open Visualization Tool (OVITO)^[35]. Topological features, i.e. nearest neighbor distances and three body labels, of this multi-lattice are included in Table 1.

order	neighbor distance	three body label
1	$\sqrt{3}a/4 \approx 0.43a$	(1, 1, 2)
2	$a/2 = 0.50a$	(1, 1, 3)
3	$\sqrt{2}a/2 \approx 0.71a$	(2, 2, 3)
4	$\sqrt{11}a/4 \approx 0.83a$	(3, 3, 3)
5	$\sqrt{3}a/2 \approx 0.87a$	(1, 2, 4)
6	$a = 1.00a$	(1, 3, 4)
7	$\sqrt{19}a/4 \approx 1.09a$	(1, 4, 4)
8	$\sqrt{5}a/2 \approx 1.12a$	(2, 4, 4)

Table 1: Neighbor distances and three body labels in the multi-lattice, up to order 8.

From this description, we can model migration pathways as static configurations on a multi-lattice. For example, for a vacancy migration in a bcc system, we can place a vacancy at the $(0, 0, 0)$ site and an atom

at the $(1/2, 1/2, 1/2)$ site. The corresponding transition state is then “semi-vacancies” at the $(0, 0, 0)$ and $(1/2, 1/2, 1/2)$ sites and an atom at the $(1/4, 1/4, 1/4)$ midpoint (Fig. 2).

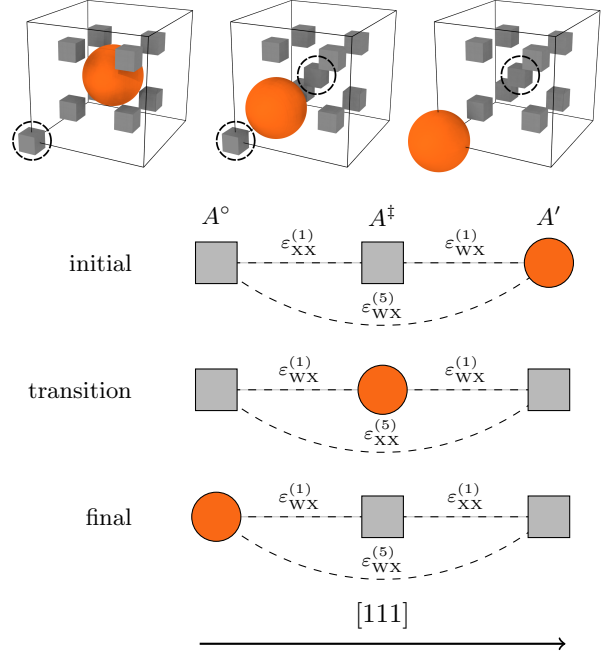


Figure 2: Vacancy migration on the bcc multi-lattice with the initial, transition, and final states with the migrating vacancy circled, with delocalization of the migrating vacancy in the transition state (top) and cartoon of migration with bond energies labeled (bottom).

Within this multi-lattice, we explicitly include the X type as an atomic type within the enumerated clusters. This is convenient for decorating transition states with feature vectors, but also allows the training to encode physical features relating to vacancies, e.g. vacancy-vacancy binding energies.

Then, for a given initial state with a vacancy at site A° and configuration tensor \mathbf{X}° , we can construct the transition and final states, respectively denoted \mathbf{X}^\ddagger and \mathbf{X}' , for a vacancy migration $\mathbf{X}^\circ \rightarrow \mathbf{X}'$:

$$\begin{aligned} \mathbf{X}^\ddagger &= \pi_1 \mathbf{X}^\circ \\ \mathbf{X}' &= (\pi_2 \circ \pi_1) \mathbf{X}^\circ \end{aligned} \quad (13)$$

where $\pi_1, \pi_2 \in S_n$ are permutations that transform the configurations by acting on the positional indices of the tensors, S_n is the symmetric group of order n , and n is the number of lattice sites within the supercell constructed with the multi-lattice. We have

adopted the convention that the right-most permutation acts first. Here, permutations $\pi \in S_n$ act on configurational tensors \mathbf{X} by means of a linear transformation:

$$(\pi \mathbf{X})_{i\alpha} = \delta_{i\pi(j)} X_{j\alpha} = X_{\pi^{-1}(i)\alpha} \quad (14)$$

Then, written in cycle notation, the permutations above are:

$$\begin{aligned} \pi_1 &= (i^\ddagger i') \\ \pi_2 &= (i^\circ i^\ddagger) \\ \pi_2 \circ \pi_1 &= (i^\circ i^\ddagger) \circ (i^\ddagger i') = (i^\circ i') \end{aligned} \quad (15)$$

where i° , i^\ddagger , and i' are respectively the indices of lattice sites A° , A^\ddagger , and A' , which are relative to the position of the migrating vacancy. This notation allows us to represent arbitrarily complex defect migration mechanisms on this fixed lattice within the canonical ensemble. Namely, the number of α types within the system is invariant under these permutations since any such π is a bijection. Additionally, the set of lattice sites that change upon this permutation is then exactly $\text{supp}(\pi)$, i.e. the support of the permutation, which can be plugged into Eq. (11) to efficiently compute feature vector differences. We save an exploration of more complex migration mechanisms using this framework for a future work.

3 Methods and Results

Using a previously developed CE model^[36], we generate structures of varying compositions, namely between 20% and 80% Ta with a 5% step. Each of these structures is then equilibrated using canonical MC implemented in within the Alloy Theoretical Automated Toolkit (ATAT)^[37] at varying temperatures, namely between 300 K and 1500 K with a 300 K step. This equilibration is merely a sampling technique, i.e. ensuring that our training set includes chemical ordering rather than solely pure samples, and could be easily replaced by a different sampling technique.

For each resulting equilibrated structure, we randomly insert a vacancy to generate an initial configuration, and move the vacancy to a random nearest neighbor to generate a final structure. To find the minimum energy path for the hop, we run NEB calculations within the Vienna Ab initio Simulation Package (VASP)^[38,39] with 5 intermediate images. Each

image is optimized using the projector augmented-wave method with Perdew-Burke-Ernzerhof exchange correlation functionals^[40] with Gaussian smearing with a width of 0.1 eV and energy cutoff of 500 eV. Electronic self-consistency was achieved with a convergence tolerance of 1×10^{-5} eV, with a minimum of 5 and a maximum of 100 electronic steps per ionic iteration. Forces were converged with a tolerance of 1×10^{-3} eV/Å. Each image has fixed cell shape and volume, i.e. only ionic positions were relaxed. An example of one of these minimum energy paths is included in Figure 3, which generates two data points to train a TCE model, namely the forward and backward hops.

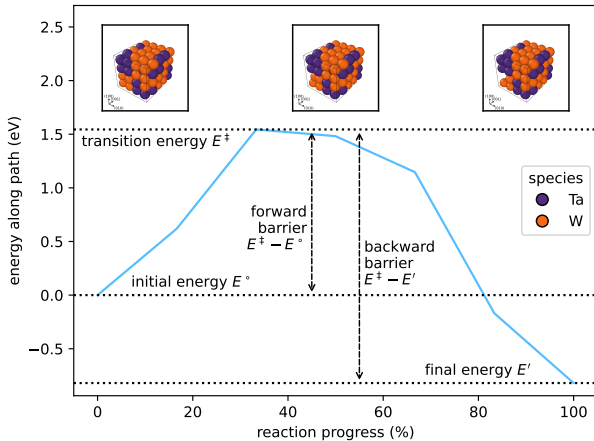


Figure 3: Example minimum energy path computed from NEB and VASP, with the initial, transition, and final states.

This example trajectory, like many other of the trajectories in the training set, exhibits strong asymmetry, i.e. the transition state lies non-negligibly far away from the midpoint of the hop. From our dataset, we additionally find that E^\ddagger is quite well correlated with $(E' + E^\circ)/2$, with an r^2 of nearly 1 and a slope of nearly 1. Namely, the KRA approximation for E^\ddagger :

$$E^\ddagger \approx E_{\text{KRA}} + \frac{E' + E^\circ}{2} \quad (16)$$

seems to be valid for our dataset. This results in the expression for the energy barrier ΔE :

$$\Delta E = E^\ddagger - E^\circ \approx E_{\text{KRA}} + \frac{E' - E^\circ}{2} \quad (17)$$

However, E_{KRA} is famously independent of direction, i.e. it is the same for both the forward reaction and its corresponding backwards reaction, so reaction asymmetry is entirely encoded in $E' - E^\circ$ within the KRA energy barrier expression in Eq. (17). Therefore, to accurately encode reaction asymmetry, it must be true that ΔE is at least moderately correlated with $E' - E^\circ$. We find that this correlation is, at best, very weak within our dataset, with a very small r^2 of 0.21 (Fig. 4).

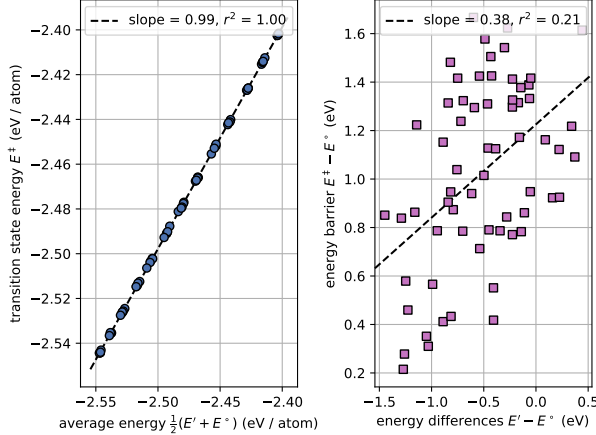


Figure 4: Transition energy E^\ddagger as a function of average energy $(E' + E^\circ)/2$ (left), and energy barrier $E^\ddagger - E^\circ$ as a function of energy difference $E' - E^\circ$ (right) from DFT + NEB calculations of vacancy hopping in Ta-W.

This means that, at least for our dataset, the energy barrier cannot be written as a function of solely $E' - E^\circ$, regardless of how those energies are computed, therefore the KRA barrier expression in Eq. (17) is insufficient for running vacancy hopping KMC for the Ta-W system. Xi et al. found a similar effect in vacancy migration in the Al-Mg-Zn alloy, in which large fluctuations of the energy barrier were largely explained by variations in E_{KRA} , rather than $E' - E^\circ$ ^[41], concluding that the standard formulation of the KRA model is insufficient for KMC simulations of vacancy diffusion in that alloy.

For our dataset, we hypothesize that this is a result of the aforementioned strong reaction pathway asymmetry within some of our data points, since the KRA relation assumes that the transition state occurs at the midpoint of the reaction. However, such a hypothesis is difficult to test, since this requires a reinterpretation of the KRA energy E_{KRA} . As such, we save this testing for a future work. Then, rather than rely on the KRA approximation to compute energy

barriers, which will quite poorly approximate energy barriers within our dataset, we will instead compute feature vectors for the initial, transition, and final states within our aforementioned multi-lattice model.

For each minimum-energy path generated by NEB above, indexed by i , we then compute the feature vectors of the initial, transition, and final configurations, respectively \mathbf{t}_i° , \mathbf{t}_i^\ddagger , and \mathbf{t}_i' , with energies E_i° , E_i^\ddagger , and E_i' . To compute feature vectors within the multi-lattice, we choose a maximum neighbor order of 8, and a maximum triplet order of 6, using a lattice parameter $a = 3.1906 \text{ \AA}$. Note that these neighbor orders are not equivalent to nearest neighbor shells on the ordinary bcc lattice, i.e. that our cluster expansion model does not sample what one would ordinarily consider to be long-range interactions. Within our multi-lattice, an 8'th nearest neighbor distance corresponds to a distance of $\sqrt{5}a/2 \approx 1.11a$. From these feature vectors, we have two training points for each path, namely:

$$\begin{aligned} p_1 &= (\Delta_f \mathbf{t}_i, \Delta_f E_i) \\ p_2 &= (\Delta_b \mathbf{t}_i, \Delta_b E_i) \end{aligned} \quad (18)$$

where $\Delta_f \mathbf{t}_i = \mathbf{t}_i^\ddagger - \mathbf{t}_i^\circ$ and $\Delta_f E_i = E_i^\ddagger - E_i^\circ$ are respectively the feature vector difference and energy barrier for the forward reaction, and $\Delta_b \mathbf{t}_i = \mathbf{t}_i^\ddagger - \mathbf{t}_i'$ and $\Delta_b E_i = E_i^\ddagger - E_i'$ are respectively the feature vector difference and energy barrier for the corresponding backward reaction. We note that this lattice parameter depends on composition, so the relaxed configurations from NEB do not exactly match our chosen lattice parameter. We address this by rescaling the supercell to have a lattice parameter equal to that of which we chose prior to computing feature vectors. Using these points, we then seek to fit a linear model using ridge regression:

$$\begin{aligned} L_f(\mathbf{j}) &= \sum_i (\Delta_f \mathbf{t}_i^\top \mathbf{j} - \Delta_f E_i)^2 \\ L_b(\mathbf{j}) &= \sum_i (\Delta_b \mathbf{t}_i^\top \mathbf{j} - \Delta_b E_i)^2 \\ L(\mathbf{j}) &= L_f(\mathbf{j}) + L_b(\mathbf{j}) + \lambda \|\mathbf{j}\|_2^2 \\ &= \|\Delta \mathbf{T} \mathbf{j} - \Delta \mathbf{e}\|_2^2 + \lambda \|\mathbf{j}\|_2^2 \\ \mathbf{j}_{\text{opt}} &= \arg \min_{\mathbf{j} \in \mathbb{R}^k} L(\mathbf{j}) \\ &= (\Delta \mathbf{T}^\top \Delta \mathbf{T} + \lambda \mathbf{I})^{-1} \Delta \mathbf{T}^\top \Delta \mathbf{e} \end{aligned} \quad (19)$$

where L_f is the loss for the forward reactions, L_b is the

loss for the backwards reactions, L is the total loss, $\lambda > 0$ is the regularization strength, $\Delta\mathbf{T}$ is the design matrix containing the feature vector differences $\Delta_f\mathbf{t}_i$ and $\Delta_b\mathbf{t}_i$ defined above, $\Delta\mathbf{e}$ is a target vector containing the energy barriers $\Delta_f E_i$ and $\Delta_b E_i$ also defined above, \mathbf{j} is the learnable matrix containing cluster interaction energies from Eq. (8), $k = 8 \cdot 3^2 + 6 \cdot 3^3 = 234$ is the feature size, i.e. the number of chosen clusters, and $\|\cdot\|_2$ denotes the L_2 norm. Note that k is not the number of linearly independent clusters, since clusters are both permutation-symmetric and subject to a one-hot occupation constraint $\sum_\alpha X_{i\alpha} = 1$. For our dataset, this count is $\text{rank}(\Delta\mathbf{T}) = 56$.

Using `scikit-learn`^[42], we first split our dataset into a training and testing set using an 80%/20% split. Then, we pick the regularization parameter λ using leave-one-out cross-validation on the training set, choosing the λ that optimizes the resulting root-mean-squared-error (RMSE), resulting in $\lambda = 23.1$.

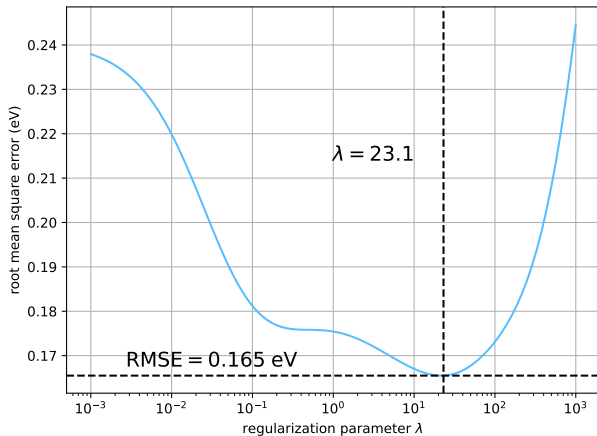


Figure 5: RMSE as a function of regularization parameter using leave-one-out cross validation.

We find that our fitted coefficients respect important physical constraints. Firstly, non-physical interactions have a resulting fitted interaction energy of 0, e.g. $\varepsilon_{\text{WW}}^{(1)}$, which describes the non-physical interaction between a W atom at a transition state site and a W atom at a nearby ordinary lattice site. Secondly, the learned coefficients respect the symmetries of each cluster type, i.e. two features that are symmetrically equivalent have the same interaction energy. This manifests as symmetry within the tensors, i.e., given any permutations $\sigma \in S_2$ and $\tau \in S_3$, the fitted interaction tensors respect the symmetry $\varepsilon_{\alpha\beta}^{(n)} = \varepsilon_{\sigma(\alpha)\tau(\beta)}^{(n)}$

and $\zeta_{\alpha\beta\gamma}^{(n)} = \zeta_{\tau(\alpha)\beta\gamma}^{(n)}$, where S_k denotes the symmetric group on k elements. Thirdly, we find that the learned two-body interaction coefficients are larger in magnitude than the learned three-body interaction coefficients. Furthermore, a small set of coefficients dominate the model. Namely, of the full set of unique clusters that satisfy the one-hot constraint, which has size $\text{rank}(\Delta\mathbf{T}) = 56$, only 21 coefficients (that are unique up to symmetry) are larger than 10 meV in magnitude (Fig. 6).

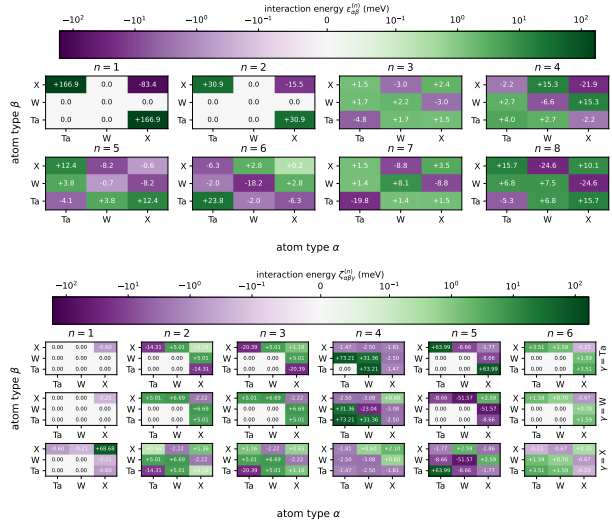


Figure 6: Pairwise interaction coefficients ε (top) and three-body interaction coefficients ζ (bottom). For the pairwise coefficients, each heatmap is labeled with an interaction order n , with each cell corresponding to a given α - β pair. For the three-body coefficients, each heatmap is labeled with an interaction order n as well as an atom type γ , with each cell corresponding to a given α - β pair. In both cases, the purple shades represent attraction, while the green shades represent repulsion, with shade corresponding to strength of the interaction.

Our fitting routine must additionally respect the constraint that a feature difference $\Delta\mathbf{t} = \mathbf{0}$ should identically evaluate to an energy difference $\Delta E = 0$. We achieve this by ensuring that our routine fits a model that does not include any intercept.

Barring a small set of outliers, we see that our model predicts the energy barriers quite well. Notably, the model performs similarly on the training and testing set, and residuals are fairly uniformly distributed about zero error. So, our model is likely not overfitted, and is likely adequately posed, i.e. it contains a sufficient number of clusters to accurately describe our energy barriers (Fig. 7).

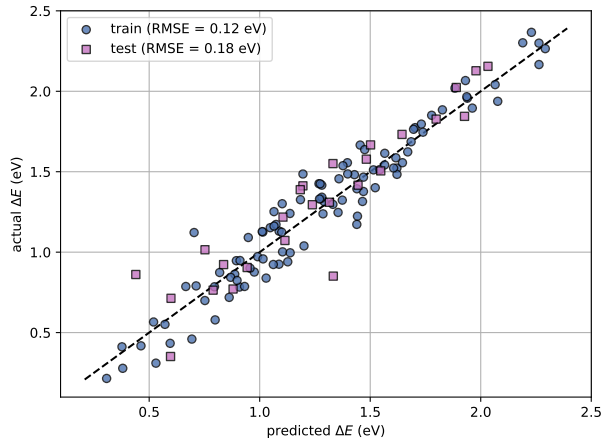


Figure 7: Parity plot of energy barrier predictions.

Lastly, the root mean square error (RMSE) in the training and testing sets, respectively 0.12 eV and 0.18 eV, are relatively small, but non-negligible. We expect this to have minimal effect on our final calculations, namely the activation energy for vacancy diffusion, but can be potentially problematic for other computations. We have elaborated on this limitation in Sec. A.1. Furthermore, these errors should be easily mitigated simply by increasing the feature space dimension, i.e. the number of considered clusters. However, our multi-lattice introduces a large feature space, namely 234 features, even for the relatively small maximum neighbor distance used in this study of $\sqrt{5}a/2 \approx 1.12a$, so introducing even more features runs a large risk of overfitting. However, many of these features are highly correlated, or even identical, suggesting that the fitting problem is well-addressed by typical dimensionality-reduction techniques such as principal component analysis (PCA). We have an exploration of such techniques for a future work.

Using our model for the energy barriers, we can simulate vacancy diffusion in varying compositions and temperatures, namely between 5% and 95% Ta and 600 K and 3000 K, and calculate diffusivity as a function of both composition and temperature. To do this, we set up a $5 \times 5 \times 5$ supercell of our multi-lattice using the Atomic Simulation Environment library^[43], and initialize one vacancy on the bcc sublattice, with energy E° . From this initial configuration, we identify the nearest atomic neighbors of the initialized vacancy. We then compute the possible transition states by moving the nearest atomic neighbors to the transition state sites sitting between them, with energies E_i^\ddagger .

Then, using `tce-lib`, we compute the feature difference between the two states, i.e. $\Delta_i \mathbf{t} = \mathbf{t}_i^\ddagger - \mathbf{t}^\circ$. This is computed using the same local difference shortcut as in our prior work^[30], which calculates feature differences solely locally, avoiding calculating redundant cluster difference counts far away from the hop. From these feature differences, we then predict the energy barrier $\Delta_i E = \mathbf{j}^\top \Delta_i \mathbf{t}$ from our fitted model above. Then, according to HTST, each rate is:

$$R_i = \nu \exp\left(-\frac{\Delta_i E}{k_B T}\right) \quad (20)$$

where ν is the rate prefactor. In this work, we set this to a constant $\nu = 1 \times 10^{13}$ Hz. Then, we choose the hopping event with probability p_i according to the residence-time algorithm^[25]:

$$p_i = \frac{R_i}{\sum_j R_j} \quad (21)$$

and we evolve the time by sampling the exponential distribution of the effective rate:

$$\Delta t \sim \text{Exp}\left(\sum_i R_i\right) \quad (22)$$

We then repeat this time-evolution step for 500,000 steps per temperature and composition. From each trajectory, we see interesting dynamics in regards to the distribution of barriers traversed over time. Namely, there seems to be a boundary in composition-temperature space in which the vacancy traverses a bimodal distribution of energy barriers, rather than a unimodal one as one might expect for a system like Ta-W, where the elements present in the solution have a large degree of chemical similarity (Fig. 8).

From the distribution of traversed barriers, we see that there are two main peaks emerging as a function of composition and temperature. For Ta-rich environments, the lower-barrier peak becomes more prominent over the high-barrier peak. This is consistent with the observation that the energy barrier for vacancy diffusion is lower in pure Ta than in pure W. From our fitted model, we have computed these barriers to be respectively $\Delta E_{\text{Ta}} = 0.84$ eV and $\Delta E_{\text{W}} = 1.97$ eV.

Interestingly, though, this relative prominence is not symmetric over composition space. For example, at

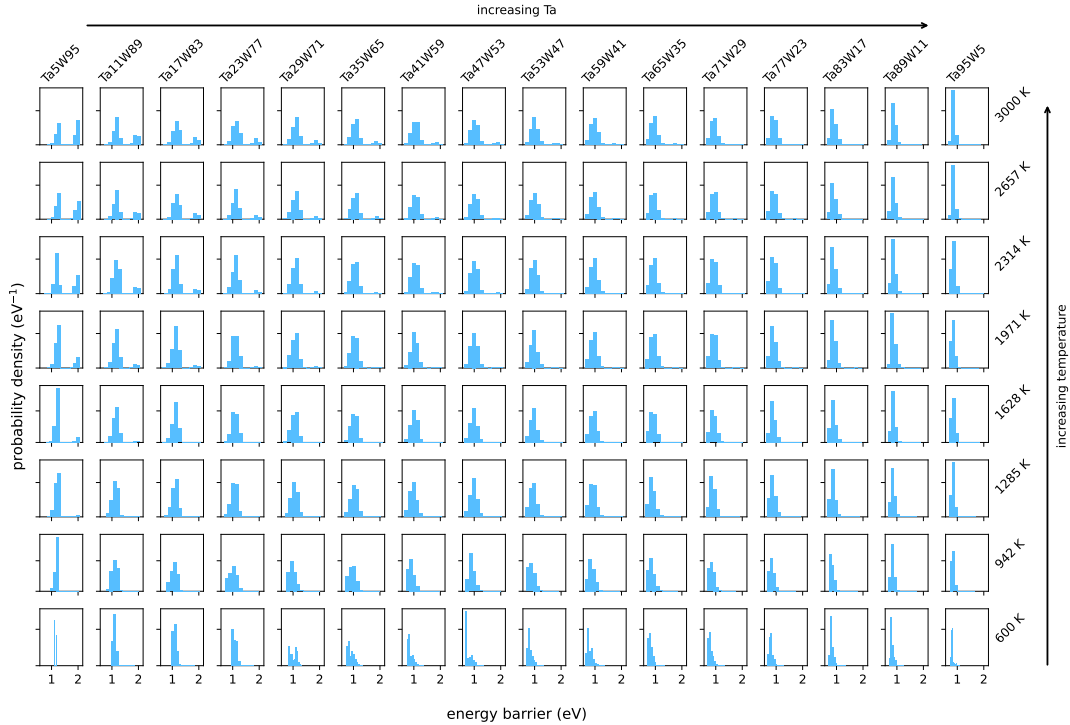


Figure 8: Distributions of traversed barriers within the KMC trajectories for each tested composition and temperature.

high temperatures in Ta-rich solutions, there is nearly no W peak. However, even in W-rich solutions, the Ta peak is quite prominent. This asymmetry is even stronger at lower temperatures, in which the W peak is not strongly present over most of the composition range. This suggests that, even at high temperatures, the vacancy is biased towards hopping in relatively Ta-rich environments, even for low Ta concentration.

From the KMC trajectories, we then compute the mean-squared displacement (MSD), for each composition and temperature, of the vacancy as a function of time t with an efficient algorithm developed by Calandri et al.^[44] that utilizes the fast Fourier transform. Then, from the MSD curves, we utilize the Einstein relation for diffusivity:

$$D = \lim_{t \rightarrow \infty} \frac{\langle \|\mathbf{r}(t_0 + t) - \mathbf{r}(t_0)\|^2 \rangle_{t_0}}{6t} \quad (23)$$

where $\langle \cdot \rangle_{t_0}$ denotes an average over possible time segments starting at t_0 , and $\mathbf{r}(t)$ is the position of the vacancy at time t . In practice, though, there are a diminishing amount of possible trajectory segments of size t as t grows. To address this, we calculate

the MSD for the entire trajectory, but linearly fit the MSD as a function of time for the first half of the data. Then, the slope of this fit is $6D$. We see that each diffusivity is well-described by the Arrhenius relation (Fig. 9):

$$D(x, T) = D_\infty(x) \exp\left(-\frac{E_a(x)}{k_B T}\right) \quad (24)$$

where $E_a(x)$ is the composition-dependent activation energy for diffusion, and $D_\infty(x)$ is the composition-dependent prefactor.

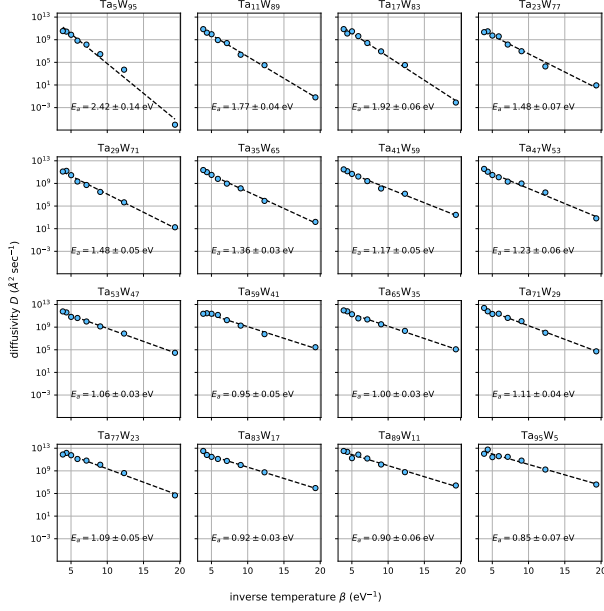


Figure 9: Predicted vacancy diffusivity as a function of composition and temperature in the Ta-W system.

From this fit, we see that the effective energy barrier roughly decreases linearly with Ta concentration for moderately concentrated solutions. This is unsurprising due to the chemical similarity between Ta and W stated above, making a Vegard’s law-like expression plausible (Fig. 10).

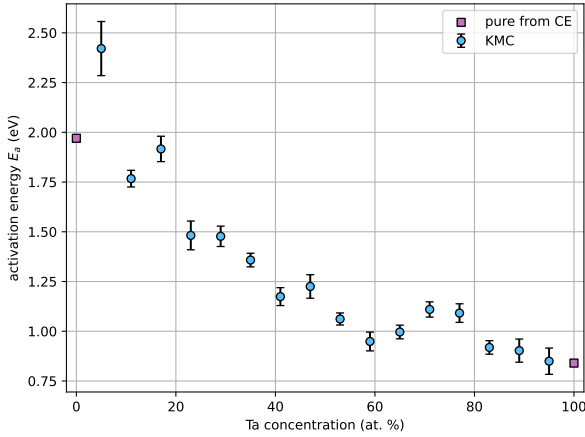


Figure 10: Predicted activation energy for vacancy diffusion as a function of composition in the Ta-W system.

However, locally, there are interesting regimes. Perhaps the most interesting is the dilute Ta region, in which dilute Ta content seems to increase the acti-

vation energy for diffusion, rather than decrease it. We attribute this to the strong preference for the vacancy to hop in Ta-rich environments, even in the W-rich region of composition space, at high temperatures, as observed in our barrier hopping distributions (Fig. 8). This is consistent with experimental work by Ipatova et al.^[45], in which they observed suppressed void growth with the addition of 5 wt % Ta to W at 800 °C, indicating hindered vacancy mobility. Our results are also consistent with thermodynamic calculations performed by Pandey et al., who showed, using the CE technique, that vacancies preferentially bind with Ta in the Ta-W system, hypothesizing that Ta clouds should slow down vacancy migration^[46]. More broadly, this is also consistent with prior descriptions of solute drag in dilute bcc alloys, in which vacancies can orbit their first nearest-neighbor sites long enough to impede long-range diffusion^[47–49]. However, beyond the dilute regime, i.e. for more than 11% Ta, we find that the vacancy’s diffusion is no longer impeded by Ta-rich orbits. In essence, when Ta is small enough in concentration, Ta can form small islands in which the vacancy orbits. Then, once Ta is large enough in concentration, these islands can percolate, supporting long-range diffusion that is enhanced by Ta.

This is consistent with the well-known bond percolation threshold in bcc solids in 3D, $p_c \approx 0.18$ ^[50]. Namely, in a random solution, the number of Ta atoms that neighbor the vacancy is binomially distributed, i.e. $N_{\text{Ta}} \sim \mathcal{B}(z, x_{\text{Ta}})$, where $z = 8$ is the coordination number of the lattice. Then, if we consider an environment to be Ta-rich if there are at least n nearest neighbor Ta atoms, we can find the region of composition space where Ta forms a percolated network by solving the inequality $P(N_{\text{Ta}} \geq n) \geq p_c$:

$$\begin{aligned}
 P(N_{\text{Ta}} \geq n) &= 1 - \sum_{k=0}^{n-1} P(N_{\text{Ta}} = k) \\
 &= 1 - \sum_{k=0}^{n-1} \binom{z}{k} x_{\text{Ta}}^k (1 - x_{\text{Ta}})^{z-k} \quad (25) \\
 &\geq p_c
 \end{aligned}$$

For $n = 2$, this yields a critical concentration $x_{\text{Ta}}^* \approx 9.8\%$, i.e. if $x_{\text{Ta}} \geq 9.8\%$, then Ta forms percolated networks. This is very consistent with our predicted effective activation energies, in which there is both a sharp drop in activation energy between 5% and 11%

Ta, as well as a relatively large increase in activation energy in 5% Ta relative to pure W. Furthermore, the standard error for the activation energy at 5% Ta is much larger than for other compositions, which is suggestive of a phase transition. From the KMC trajectories, we additionally find that the average excess Ta near the vacancy generally increases with W concentration, with more excess at lower temperatures (Fig. 11). We define this excess as:

$$\Gamma_{\text{Ta}} = \frac{\langle \phi_{\text{Ta}} \rangle - x_{\text{Ta}}}{x_{\text{Ta}}} \quad (26)$$

where $\langle \phi_{\text{Ta}} \rangle$ is the average fraction of Ta atoms within the local environment of the hopping vacancy, which we take to be the first and second nearest neighbor shells. Then, if $\Gamma_{\text{Ta}} > 0$, the vacancy on average spends more time near Ta atoms than if the vacancy had no bias towards orbiting near any atom type.

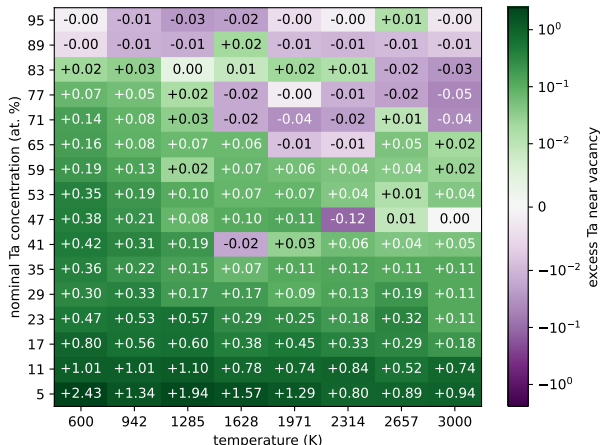


Figure 11: Ta excess near vacancy Γ_{Ta} throughout the KMC simulations. Each cell represents a simulation at a fixed temperature and nominal composition. The purple shades represent attraction of the vacancy to Ta, i.e. excess Ta, while the green shades represent repulsion, i.e. depleted Ta, with shade corresponding to magnitude of excess/depletion.

The results for excess Ta near the vacancy are consistent with the percolation picture, i.e., for small Ta concentrations, the vacancy is biased towards Ta-rich environments, inhibiting diffusion.

We find that dilute W does not have a similar effect in pure Ta. Namely, dilute W does not significantly change the activation energy for vacancy diffusion. Within this regime, the distributions of visited energy barriers are very similar, with no visible W peak until about 60% W at high temperatures.

Then, in the regime where Ta is concentrated enough to form percolated networks but the alloy remains majority W (11% to 59% Ta), we find that Ta enhances diffusion. We attribute this to something more trivial, wherein Ta enhances diffusion from energetics alone, but W is sufficiently present such that hops in W-rich environments are no longer avoidable, yielding a regime in which a mean-field-theory picture is appropriate. This can also be seen in the traversed barrier distributions, in which there is a smaller, but significant W-peak at high temperatures within this composition range.

4 Discussion

The ability to accurately predict diffusion in concentrated alloys remains a central challenge in computational materials science, owing to the strong dependence of migration barriers on the local chemical environment. Traditional approaches often rely on simplified kinetic models, such as the KRA approximation, or assume a small number of representative barriers, which can obscure the role of local configurational variability in governing transport.

From a practical standpoint, this framework enables predictive first-principles modeling of diffusion in multicomponent alloys without relying on ad hoc kinetic approximations. In particular, it opens the door to high-throughput screening of alloy compositions with tailored transport properties, as well as the investigation of complex phenomena such as solute drag, percolation of fast diffusion pathways, and composition-dependent activation energies. More broadly, the methodology is general and can be extended to other defect-mediated processes, including self-interstitial diffusion and defect clustering, provided that the relevant transition-state energetics are adequately sampled. As such, this work establishes a physically consistent and rigorous framework for bridging first-principles calculations and mesoscale kinetics in chemically complex materials, with potential applications spanning alloy design, irradiation response, and high-temperature materials performance.

Beyond predictive capability, though, the present framework also enables new avenues for engineering diffusion in concentrated alloys. By explicitly resolving the distribution of migration barriers and their dependence on local chemical environments, diffusion can be understood in terms of the connectivity of low-barrier pathways on the lattice. This provides a nat-

ural route to tuning transport via percolation: alloy compositions may be designed to either promote or suppress the formation of connected networks of fast diffusion channels, thereby controlling overall mobility.

Similarly, the framework provides a quantitative description of solute drag as an emergent consequence of local barrier statistics, enabling the identification of compositions that inhibit or enhance vacancy motion. These effects have direct implications for high-temperature performance and radiation response, where vacancy mobility governs processes such as creep and void growth. In particular, suppressing the percolation of low-barrier pathways or enhancing trapping environments offers a potential strategy for reducing vacancy flux and mitigating void formation. For applications where we might be interested in inhibiting diffusion, e.g. minimizing void growth, this work then suggests that dilute Ta is optimal. On the other hand, for applications where we might be interested in enhancing diffusion, e.g. increasing vacancy flux towards a defect sink to annihilate vacancies, one can then engineer percolated networks simply by having a Ta concentration larger than $x_{\text{Ta}} \approx 9.8\%$. This drag effect also indicates that, in the Ta-W system, Ta should segregate near point defect sinks. We additionally hypothesize that this dragging/percolation effect should hold for other solutes in which vacancy migration barriers are locally lowered. For example, first-principles studies show that Re and Os have lower vacancy-mediated diffusion barriers in W than W’s self diffusion barrier^[51–53]. This effect could therefore be relevant in studying how kinetically-controlled properties of plasma-facing W armor in fusion reactors, in which transmutation via neutron irradiation yields roughly 3.8% Re and 1.4% Os in pure W over a period of five years^[54], evolve over the lifetime of the materials in irradiated environments.

More broadly, by directly learning environment-dependent migration barriers from first-principles data, the present approach avoids the need for reduced kinetic models such as the KRA approximation. This enables a unified and systematically improvable framework for modeling diffusion across a wider class of chemically complex materials, where local environments and transition-state energetics cannot be captured by simplified parameterizations.

5 Limitations and future work

Migration rates in this work are evaluated within the framework of HTST, in which the activation free energy is approximated by the difference in potential energy between the transition and initial states. This approximation is formally valid in the low-temperature limit, where vibrational free energy contributions are assumed to be harmonic and largely cancel between configurations. At elevated temperatures, however, entropic effects can become non-negligible. In particular, vibrational entropy differences between the initial and transition states, as well as anharmonic contributions, can lead to significant deviations from Arrhenius behavior. Recent studies in W have demonstrated that migration free energies exhibit strong temperature dependence due to anharmonic vibrational effects, resulting in measurable non-Arrhenius diffusion behavior^[55]. These results suggest that a purely energetic description of migration barriers may neglect important finite-temperature contributions.

Nevertheless, the cluster expansion formalism employed here can, in principle, be extended to incorporate vibrational contributions. For example, temperature-dependent effective cluster interactions may be constructed by fitting to free energies rather than energies, enabling the inclusion of vibrational entropy within the same expansion framework^[56,57]. Such extensions provide a systematic route toward incorporating finite-temperature effects beyond the HTST approximation.

Additionally, the KMC simulations performed in this work sample configurations that are, to a good approximation, representative of a random solid solution. While local compositional fluctuations naturally arise from vacancy-mediated dynamics, the system does not exhibit significant evolution toward ordered states over the timescales considered. As such, the underlying ensemble remains close to a disordered configuration throughout the simulations. In general, SRO can have a nontrivial impact on diffusion kinetics by modifying the local chemical environment encountered by migrating defects. Changes in SRO alter the distribution of migration barriers, potentially leading to variations in effective diffusivities and activation energies. In particular, the emergence of preferred local motifs may either facilitate or hinder vacancy motion depending on the associated energetics.

However, the temperatures considered in this study

lie well above the order-disorder transition temperature (ODTT) of the Ta-W system, which has been estimated to fall in the range of 200 K to 400 K^[15]. Therefore, for our temperature range (600 K-3000 K), equilibrium configurations are expected to exhibit minimal SRO, and the assumption of a random solid solution is therefore well justified. Consequently, the influence of ordering on the computed diffusion properties is expected to be limited under the present conditions.

We note, however, that at lower temperatures approaching the ODTT, or in systems with stronger ordering tendencies, SRO could play a more significant role in determining diffusion behavior. In such cases, a fully coupled treatment of thermodynamics and kinetics would be required to accurately capture the interplay between ordering and transport. This is especially relevant for studying percolation effects, in which it has been recently shown that percolation thresholds can strongly depend on chemical SRO in binary alloys^[58-61].

Thirdly, the KMC simulations in this work are performed on finite supercells (bcc $5 \times 5 \times 5$), which may introduce finite-size effects. In particular, small systems may suppress long-wavelength compositional fluctuations or introduce weak correlations through periodic boundary conditions. Additionally, the diversity of local environments sampled by the vacancy may be reduced in smaller supercells, potentially affecting the statistics of rare configurations. That said, such effects are typically most pronounced in systems involving long-range interactions, defect clustering, or spatially extended phenomena.

For the present case of dilute vacancy diffusion in a disordered solid solution, where kinetics are governed primarily by local environments and short-range energetics, these finite-size effects are expected to be limited. Nevertheless, systematic finite-size scaling could be employed in future work to further quantify any residual size dependence of the computed diffusivities.

Lastly, the KMC simulations in this work are performed in the dilute-defect limit, with a single vacancy evolving within the simulation cell. As such, interactions between multiple vacancies, including vacancy-vacancy binding and clustering, are not explicitly considered. These effects can become important at elevated defect concentrations, where the formation of vacancy clusters, voids, or extended defects

may kinetically trap vacancies and, in turn, affect mechanical properties such as swelling, creep, and irradiation response. In the present context, the single-vacancy approximation enables a focused investigation of the local chemical factors governing migration barriers and diffusivity in a disordered solid solution. For sufficiently low equilibrium vacancy concentrations, this approximation is expected to provide an accurate description of tracer-like diffusion behavior.

We note, however, that the framework developed here is not inherently restricted to the single-vacancy limit. In principle, the same training set could be augmented to include multiple vacancies, providing vacancy-vacancy and higher-order defect interactions within the training data. Such an approach would enable the study of vacancy clustering kinetics and collective diffusion phenomena within a consistent atomistic framework.

6 Conclusions

In this work, we have extended our prior work on TCE models by augmenting the lattice with transition state sites, embedding transition states for vacancy migration into configuration space, allowing us to treat transition states as distinct configurations within configuration space. We then use this construction to fit vacancy migration barriers in the Ta-W alloy, showing that this allows us to accurately predict the energy barrier of a vacancy hop in Ta-W as a function of features local to the hop without the use of the KRA relation.

We then use this fitted model to simulate vacancy diffusion using a KMC methodology. From the resulting diffusion data, we argue that vacancy diffusion follows 3 distinct regimes:

- Dilute Ta ($0\% \leq x_{\text{Ta}} \leq 5\%$), in which Ta acts as a dragging solute
- Moderate Ta ($11\% \leq x_{\text{Ta}} \leq 59\%$), in which Ta still dominates diffusion, but forms percolated networks that support long-range diffusion
- Moderate to dilute W ($64\% \leq x_{\text{Ta}} \leq 100\%$), in which the vacancy avoids W, exhibiting diffusion similar to pure Ta

More generally, this work enables the combination of first-principles transition-state energetics with data-driven cluster expansions beyond the KRA approximation, further enabling a physically transparent

and computationally efficient framework for predicting diffusion in complex alloys, providing a foundation for both mechanistic understanding of diffusion, and therefore materials design, for advanced applications.

7 Data Availability

Excluding the raw VASP and NEB data, all data and code necessary to replicate this study is available on GitHub^[62]. Raw VASP data has been excluded to avoid copyright issues, but will be made available upon reasonable and legal request.

8 Acknowledgements

Authors acknowledge support from the U.S. Department of Energy, Office of Basic Energy Sciences, Materials Science and Engineering Division under Award No. DE-SC0022980.

Additionally, this material is based on work supported by the National Science Foundation under Grant Nos. MRI# 2024205, MRI# 1725573, and CRI# 2010270 for allotment of compute time on the Clemson University Palmetto Cluster.

9 Disclaimer

Any opinions, findings, and conclusions or recommendations expressed in this material are those of the author(s) and do not necessarily reflect the views of the National Science Foundation.

A Appendix

A.1 Energy barrier error propagation

Suppose the true energy barrier is ΔE° , but we predict an energy barrier $\Delta E = \Delta E^\circ + \varepsilon$, where $\varepsilon \sim \mathcal{N}(0, \sigma^2)$ is normally distributed. We then predict a rate, on average:

$$\begin{aligned} \langle \hat{r} \rangle &= \nu \exp\left(-\frac{\Delta E^\circ}{k_B T}\right) \left\langle \exp\left(-\frac{\varepsilon}{k_B T}\right) \right\rangle \\ &= r_{\text{true}} \exp\left(\frac{\sigma^2}{2(k_B T)^2}\right) \end{aligned} \quad (27)$$

where $r_{\text{true}} = \nu \exp\left(-\frac{\Delta E^\circ}{k_B T}\right)$ is the true rate and $\langle \hat{r} \rangle$ is the average predicted rate. Then, the error blows up exponentially, both with inverse temperature and prediction variance σ^2 . For test RMSE 0.2 eV at temperature 500 K, this amounts to roughly $\exp\left(\frac{\sigma^2}{2(k_B T)^2}\right) \approx 5 \times 10^4$, i.e. 4-5 orders of magnitude difference. We expect that this has minimal effect on computing quantities like the activation energy, which are proportional to $\ln \hat{r} \propto -\frac{\varepsilon}{k_B T}$. However, for computing absolute diffusivities, it might be necessary to estimate rates with a different strategy. Two possible solutions might be correcting the predicted rates by $\exp\left(\frac{\sigma^2}{2(k_B T)^2}\right)$, or by fitting rates directly rather than energy barriers. We save an exploration of these strategies for a future work.

References

- [1] Songqin Xia, Michael C Gao, Tengfei Yang, Peter K Liaw, and Yong Zhang. Phase stability and microstructures of high entropy alloys ion irradiated to high doses. *Journal of Nuclear Materials*, 480:100–108, 2016.
- [2] Chenyang Lu, Liangliang Niu, Nanjun Chen, Ke Jin, Taini Yang, Pengyuan Xiu, Yanwen Zhang, Fei Gao, Hongbin Bei, Shi Shi, et al. Enhancing radiation tolerance by controlling defect mobility and migration pathways in multicomponent single-phase alloys. *Nature communications*, 7(1):13564, 2016.
- [3] Fredric Granberg, K Nordlund, Mohammad W Ullah, Ke Jin, Chenyang Lu, Hongbin Bei, LM Wang, F Djurabekova, WJ Weber, and Y Zhang. Mechanism of radiation damage reduction in equiatomic multicomponent single phase alloys. *Physical review letters*, 116(13):135504, 2016.
- [4] Michael Nastasi and James W Mayer. Thermodynamics and kinetics of phase transformations induced by ion irradiation. *Materials science reports*, 6(1):1–51, 1991.
- [5] M Nastar and F Soisson. 1.18-Radiation-induced segregation. *Comprehensive nuclear materials*, 1:471–496, 2012.
- [6] Ludovic Thuiet, M Nastar, E Martinez, GF Bouobda Moladje, Alexandre Legris, and F Soisson. Multiscale modeling of radiation in-

- duced segregation in iron based alloys. *Computational Materials Science*, 149:324–335, 2018.
- [7] H Wiedersich, PR Okamoto, and Nghi Q Lam. A theory of radiation-induced segregation in concentrated alloys. *Journal of Nuclear Materials*, 83(1):98–108, 1979.
- [8] Z Jiao and GS Was. Novel features of radiation-induced segregation and radiation-induced precipitation in austenitic stainless steels. *Acta Materialia*, 59(3):1220–1238, 2011.
- [9] E Meslin, Bertrand Radiguet, and M Loyer-Prost. Radiation-induced precipitation in a ferritic model alloy: An experimental and theoretical study. *Acta Materialia*, 61(16):6246–6254, 2013.
- [10] R Cauvin and G Martin. Solid solutions under irradiation. II. Radiation-induced precipitation in AlZn undersaturated solid solutions. *Physical Review B*, 23(7):3333, 1981.
- [11] Oleg N Senkov, GB Wilks, DB Miracle, CP Chuang, and PK Liaw. Refractory high-entropy alloys. *Intermetallics*, 18(9):1758–1765, 2010.
- [12] Oleg N Senkov, Garth B Wilks, James M Scott, and Daniel B Miracle. Mechanical properties of Nb₂₅Mo₂₅Ta₂₅W₂₅ and V₂₀Nb₂₀Mo₂₀Ta₂₀W₂₀ refractory high entropy alloys. *Intermetallics*, 19(5):698–706, 2011.
- [13] Osman El-Atwani, Nan Li, Meimei Li, Arun Devaraj, Jon Kevin Scott Baldwin, Matthew M Schneider, Damian Sobieraj, Jan S Wróbel, Duc Nguyen-Manh, Stuart A Maloy, et al. Outstanding radiation resistance of tungsten-based high-entropy alloys. *Science advances*, 5(3):eaav2002, 2019.
- [14] Osman El Atwani, Hi T Vo, Matheus Araujo Tunes, Chanhoo Lee, A Alvarado, N Krienke, Jonathan D Poplawsky, Aaron A Kohnert, Jonathan Gigax, W-Y Chen, et al. A quinary WTaCrVHf nanocrystalline refractory high-entropy alloy withholding extreme irradiation environments. *Nature communications*, 14(1):2516, 2023.
- [15] Bochuan Sun, Mark Fedorov, Jan Wrobel, Duc Nguyen-Manh, Caleb Hatler, Matthew Vigil, Dan J Thoma, Osman El-Atwani, and Enrique Martinez. Thermodynamic assessment of the quaternary WTaCrV refractory high entropy alloy as a means to guide experimental approaches. *Acta Materialia*, page 121435, 2025.
- [16] Yi-Zhou Wang and Yun-Jiang Wang. Disentangling diffusion heterogeneity in high-entropy alloys. *Acta Materialia*, 224:117527, 2022.
- [17] Shijun Zhao. Role of chemical disorder and local ordering on defect evolution in high-entropy alloys. *Physical Review Materials*, 5(10):103604, 2021.
- [18] A. Van der Ven, G. Ceder, M. Asta, and P. D. Tepesch. First-principles theory of ionic diffusion with nondilute carriers. *Phys. Rev. B*, 64:184307, Oct 2001.
- [19] A. Van der Ven and G. Ceder. First principles calculation of the interdiffusion coefficient in binary alloys. *Phys. Rev. Lett.*, 94:045901, Feb 2005.
- [20] Xi Zhang and Marcel HF Sluiter. Kinetically driven ordering in phase separating alloys. *Phys. Rev. Mater*, 3(9):095601, 2019.
- [21] Anton Van der Ven, John C Thomas, Brian Puchala, and Anirudh Raju Natarajan. First-principles statistical mechanics of multicomponent crystals. *Annual Review of Materials Research*, 48(1):27–55, 2018.
- [22] Didier De Fontaine. Cluster approach to order-disorder transformations in alloys. In *Solid state physics*, volume 47, pages 33–176. Elsevier, 1994.
- [23] Pierre Hohenberg and Walter Kohn. Inhomogeneous electron gas. *Physical review*, 136(3B):B864, 1964.
- [24] Walter Kohn and Lu Jeu Sham. Self-consistent equations including exchange and correlation effects. *Physical review*, 140(4A):A1133, 1965.
- [25] Alfred B Bortz, Malvin H Kalos, and Joel L Lebowitz. A new algorithm for monte carlo simulation of ising spin systems. *Journal of Computational physics*, 17(1):10–18, 1975.
- [26] Graeme Henkelman and Hannes Jónsson. Improved tangent estimate in the nudged elastic band method for finding minimum energy paths and saddle points. *The Journal of chemical physics*, 113(22):9978–9985, 2000.

- [27] Graeme Henkelman, Blas P Uberuaga, and Hannes Jónsson. A climbing image nudged elastic band method for finding saddle points and minimum energy paths. *The Journal of chemical physics*, 113(22):9901–9904, 2000.
- [28] Aiichiro Nakano. A space–time-ensemble parallel nudged elastic band algorithm for molecular kinetics simulation. *Computer Physics Communications*, 178(4):280–289, 2008.
- [29] Emile Maras, Oleg Trushin, Alexander Stukowski, Tapio Ala-Nissila, and Hannes Jónsson. Global transition path search for dislocation formation in Ge on Si (001). *Computer Physics Communications*, 205:13–21, 2016.
- [30] Jacob Jeffries, Bochuan Sun, and Enrique Martinez. A generalized and adaptable tensor-contraction-based cluster expansion formalism for multicomponent solids. *Computational Materials Science*, 262:114338, 2026.
- [31] Henry Eyring. The activated complex and the absolute rate of chemical reactions. *Chemical Reviews*, 17(1):65–77, 1935.
- [32] Md Rajib Khan Musa, Yichen Qian, Jie Peng, and David Cereceda. Accelerating the discovery of low-energy structure configurations: A computational approach that integrates first-principles calculations, Monte Carlo sampling, and Machine Learning. *Scripta Materialia*, 259:116535, 2025.
- [33] Arthur F Voter. Introduction to the kinetic Monte Carlo method. In *Radiation effects in solids*, pages 1–23. Springer, 2007.
- [34] Yasuhiro Oda, Atsushi M Ito, Arimichi Takayama, and Hiroaki Nakamura. First-principles study on migration of vacancy in tungsten. *Plasma and Fusion Research*, 9:3401117–3401117, 2014.
- [35] Alexander Stukowski. Visualization and analysis of atomistic simulation data with OVITO—the Open Visualization Tool. *Modelling and Simulation in Materials Science and Engineering*, 18(1), Jan 2010.
- [36] Andrew M Alvarado, Chanhoo Lee, Jan S Wróbel, Damian Sobieraj, Duc Nguyen-Manh, Jonathan D Poplawsky, Saryu Jindal Fensin, Enrique Martinez, and Osman El-Atwani. Predicting short-range order evolution in WTaCrVHF refractory high-entropy alloys. *Scripta materialia*, 233:115506, 2023.
- [37] Axel Van De Walle, Mark Asta, and Gerbrand Ceder. The alloy theoretic automated toolkit: A user guide. *Calphad*, 26(4):539–553, 2002.
- [38] Georg Kresse and Jürgen Hafner. Ab initio molecular dynamics for liquid metals. *Physical review B*, 47(1):558, 1993.
- [39] Georg Kresse and Jürgen Furthmüller. Efficient iterative schemes for ab initio total-energy calculations using a plane-wave basis set. *Physical review B*, 54(16):11169, 1996.
- [40] John P Perdew, Kieron Burke, and Matthias Ernzerhof. Generalized gradient approximation made simple. *Physical review letters*, 77(18):3865, 1996.
- [41] Zhucong Xi, Mingfei Zhang, Louis G Hector Jr, Amit Misra, and Liang Qi. Mechanism of local lattice distortion effects on vacancy migration barriers in fcc alloys. *Physical Review Materials*, 6(7):073601, 2022.
- [42] F. Pedregosa, G. Varoquaux, A. Gramfort, V. Michel, B. Thirion, O. Grisel, M. Blondel, P. Prettenhofer, R. Weiss, V. Dubourg, J. Vanderplas, A. Passos, D. Cournapeau, M. Brucher, M. Perrot, and E. Duchesnay. Scikit-learn: Machine learning in Python. *Journal of Machine Learning Research*, 12:2825–2830, 2011.
- [43] Ask Hjorth Larsen, Jens Jørgen Mortensen, Jakob Blomqvist, Ivano E Castelli, Rune Christensen, Marcin Dułak, Jesper Friis, Michael N Groves, Bjørk Hammer, Cory Hargus, Eric D Hermes, Paul C Jennings, Peter Bjerre Jensen, James Kermode, John R Kitchin, Esben Leonhard Kolsbjerg, Joseph Kubal, Kristen Kaasbjerg, Steen Lysgaard, Jón Bergmann Maronsson, Tristan Maxson, Thomas Olsen, Lars Pastewka, Andrew Peterson, Carsten Rostgaard, Jakob Schiøtz, Ole Schütt, Mikkel Strange, Kristian S Thygesen, Tejs Vegge, Lasse Vilhelmsen, Michael Walter, Zhenhua Zeng, and Karsten W Jacobsen. The atomic simulation environment—a Python library for working with atoms. *Journal of Physics: Condensed Matter*, 29(27):273002, 2017.
- [44] Vania Calandrini. nMoldyn-Interfacing spectroscopic experiments, molecular dynamics simula-

- tions and models for time correlation functions. *École thématique de la Société Française de la Neutronique*, 2011.
- [45] Iuliia Ipatova, RW Harrison, SE Donnelly, MJD Rushton, SC Middleburgh, and Enrique Jimenez-Melero. Void evolution in tungsten and tungsten-5wt.% tantalum under in-situ proton irradiation at 800 and 1000 c. *Journal of Nuclear Materials*, 526:151730, 2019.
- [46] Dhanshree Pandey, Kalle Heinola, Christian Hill, and Nicola Seriani. Synergistic insights into the tungsten-tantalum-vacancy system: A DFT-cluster expansion study. *Computational Materials Science*, 251:113718, 2025.
- [47] Thomas Garnier, Maylise Nastar, Pascal Bellon, and Dallas R Trinkle. Solute drag by vacancies in body-centered cubic alloys. *Phys. Rev. B*, 88(13):134201, 2013.
- [48] Luca Messina, Maylise Nastar, Thomas Garnier, Christophe Domain, and Pär Olsson. Exact ab initio transport coefficients in bcc Fe-X (X= Cr, Cu, Mn, Ni, P, Si) dilute alloys. *Physical Review B*, 90(10):104203, 2014.
- [49] Luca Messina, Maylise Nastar, Nils Sandberg, and Pär Olsson. Systematic electronic-structure investigation of substitutional impurity diffusion and flux coupling in bcc iron. *Physical Review B*, 93(18):184302, 2016.
- [50] Christian D Lorenz and Robert M Ziff. Precise determination of the bond percolation thresholds and finite-size scaling corrections for the sc, fcc, and bcc lattices. *Physical Review E*, 57(1):230, 1998.
- [51] T Suzudo, M Yamaguchi, and Akira Hasegawa. Stability and mobility of rhenium and osmium in tungsten: first principles study. *Modelling and Simulation in Materials Science and Engineering*, 22(7):075006, 2014.
- [52] Yu-Hao Li, Hong-Bo Zhou, Shuo Jin, Ying Zhang, Huiqiu Deng, and Guang-Hong Lu. Behaviors of transmutation elements Re and Os and their effects on energetics and clustering of vacancy and self-interstitial atoms in W. *Nuclear Fusion*, 57(4):046006, 2017.
- [53] Yuhao Li, Fangfei Ma, Fangya Yue, Qingyuan Ren, Hongbo Zhou, and Guanghong Lu. Radiation-induced precipitation of transmutation elements rhenium/osmium and their effects on hydrogen behavior in tungsten. *Progress in Natural Science: Materials International*, 29(3):285–294, 2019.
- [54] MR Gilbert and J-Ch Sublet. Neutron-induced transmutation effects in W and W-alloys in a fusion environment. *Nuclear Fusion*, 51(4):043005, 2011.
- [55] Xi Zhang, Sergiy V Divinski, and Blazej Grabowski. Ab initio machine-learning unveils strong anharmonicity in non-Arrhenius self-diffusion of tungsten. *Nature Communications*, 16(1):394, 2025.
- [56] Maximilien Levesque, Enrique Martinez, Chu-Chun Fu, Maylise Nastar, and Frédéric Soisson. Simple concentration-dependent pair interaction model for large-scale simulations of Fe-Cr alloys. *Physical Review B—Condensed Matter and Materials Physics*, 84(18):184205, 2011.
- [57] Enrique Martínez, Oriane Senninger, Chu-Chun Fu, and Frédéric Soisson. Decomposition kinetics of Fe-Cr solid solutions during thermal aging. *Physical Review B—Condensed Matter and Materials Physics*, 86(22):224109, 2012.
- [58] Ge Yu. Correlated percolation in solid solutions with short-range order. *Philosophical Magazine B*, 69(1):95–101, 1994.
- [59] Megan E Frary and Christopher A Schuh. Correlation-space description of the percolation transition in composite microstructures. *Physical Review E—Statistical, Nonlinear, and Soft Matter Physics*, 76(4):041108, 2007.
- [60] Abhinav Roy, Karl Sieradzki, James M Rondinelli, and Ian D McCue. Effect of chemical short-range order and percolation on passivation in binary alloys. *Physical Review B*, 110(8):085420, 2024.
- [61] Abhinav Roy, Karl Sieradzki, Michael J. Waters, James M. Rondinelli, and Ian McCue. Percolation diagrams derived from first-principles investigation of chemical short-range order in binary alloys. *Scripta Materialia*, 274:117137, 2026.
- [62] MUEXLY Research Group. TaW-tce-kmc. <https://github.com/MUEXLY/TaW-tce-kmc>, 2026. GitHub repository, accessed 2026-04-17.